Classification of SD-OCT Volumes using Local Binary Patterns: Experimental Validation for DME Detection

Guillaume Lemaître[1,a,*], Mojdeh Rastgoo[1,a,*], Joan Massich[1,*], Carol Y. Cheung[c], Tien Y. Wong[c], Ecosse Lamoureux[c], Dan Milea[c], Fabrice Mériaudeau[1], Désiré Sidibé[1]

[a]*ViCOROB, Universitat de Girona, Campus Montilivi, Edifici P4, 17071 Girona, Spain*
[b]*LE2I UMR6306, CNRS, Arts et Métiers, Univ. Bourgogne Franche-Comté, 12 rue de la Fonderie, 71200 Le Creusot, France*
[c]*Singapore Eye Research Institute, Singapore National Eye Center, Singapore*

Abstract

This paper addresses the problem of automatic classification of Spectral Domain OCT (SD-OCT) data for automatic identification of patients with Diabetic Macular Edema (DME) versus normal subjects. Optical Coherence Tomography (OCT) has been a valuable diagnostic tool for DME, which is among the most common causes of irreversible vision loss in individuals with diabetes. Here, a classification framework with five distinctive steps is proposed and we present an extensive study of each step. Our method considers combination of various pre-processings in conjunction with Local Binary Patterns (LBP) features and different mapping strategies. Using linear and non-linear classifiers, we tested the developed framework on a balanced cohort of 32 patients.

Experimental results show that the proposed method outperforms the previous studies by achieving a Sensitivity (SE) and Specificity (SP) of 81.2% and 93.7%, respectively. Our study concludes that the 3D features and high-level representation of 2D features using patches achieve the best results. However, the effects of pre-processing is inconsistent with respect to different classifiers

---

[☆]Document source available in GitHub [1]

[*]Corresponding author

Email addresses: g.lemaitre58@gmail.com (Guillaume Lemaître), mojdeh.rastgoo@gmail.com (Mojdeh Rastgoo), joan.massich@u-bourgogne.fr (Joan Massich)

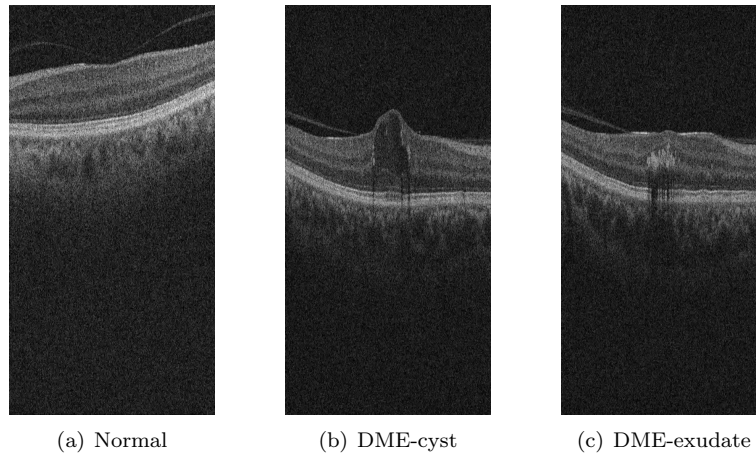(a) Normal   (b) DME-cyst   (c) DME-exudate

Figure 1: Example of SD-OCT images for normal (a) and DME patients (b)-(c) with cyst and exudate, respectively.

and feature configurations.

Keywords: Diabetic Macular Edema, Optical Coherence Tomography, DME, OCT, LBP

1. Introduction

Eye diseases such as Diabetic Retinopathy (DR) and Diabetic Macular Edema (DME) are the most common causes of irreversible vision loss in individuals with diabetes. Just in United States alone, health care and associated costs related to eye diseases are estimated at almost \$500 M [2]. Moreover, the prevalent cases of DR are expected to grow exponentially affecting over 300 M people worldwide by 2025 [3]. Given this scenario, early detection and treatment of DR and DME play a major role to prevent adverse effects such as blindness. DME is characterized as an increase in retinal thickness within 1 disk diameter of the fovea center with or without hard exudates and sometimes associated with cysts [4]. Fundus images which have proven to be very useful in revealing most of the eye pathologies [5, 6] are not as good as Optical Coherence Tomography (OCT) images which provide information about cross-sectional retinal morphology [7].

2

Many of the previous works on OCT image analysis have focused on the problem of retinal layers segmentation, which is a necessary step for retinal thickness measurements [9, 10]. However, few have addressed the specific problem of DME and its associated features detection from OCT images. Figure 1 shows one normal B-scan and two abnormal B-scans.

A summary of the existing work can be found in Table 1. Srinivasan *et al.* [11] proposed a classification method to distinguish DME, Age-related Macular Degeneration (AMD) and normal SD-OCT volumes. The OCT images are pre-processed by reducing the speckle noise by enhancing the sparsity in a transform-domain and flattening the retinal curvature to reduce the inter-patient variations. Then, Histogram of Oriented Gradients (HOG) are extracted for each slice of a volume and a linear Support Vector Machines (SVM) is used for classification. On a dataset of 45 patients equally subdivided into the three aforementioned classes, this method leads to a correct classification rate of 100%, 100% and 86.67% for normal, DME and AMD patients, respectively. The images that have been used in their paper, are publicly available but are already preprocessed (i.e., denoised), have different sizes for the OCT volumes, do not offer a huge variability in term of DME lesions, and some of them, without specifying which, have been excluded for the training phase; all these reasons prevent us from using this dataset to benchmark our work.

Venhuizen *et al.* proposed a method for OCT images classification using the Bag-of-Words (BoW) models [12]. The method starts with the detection and selection of keypoints in each individual B-scan, by keeping the most salient points corresponding to the top 3% of the vertical gradient values. Then, a texton of size 9×9 pixels is extracted around each keypoint, and Principal Component Analysis (PCA) is applied to reduce the dimension of every texton to get a feature vector of size 9. All extracted feature vectors are used to create a codebook using k-means clustering. Then, each OCT volume is represented in terms of this codebook and is characterized as a histogram that captures the codebook occurrences. These histograms are used as feature vector to train a Random Forest (RF) with a maximum of 100 trees. The method was used to

3

classify OCT volumes between AMD and normal cases and achieved an Area Under the Curve (AUC) of 0.984 with a dataset of 384 OCT volumes.

Liu *et al.* proposed a methodology for detecting macular pathology in OCT images using Local Binary Patterns (LBP) and gradient information as attributes [13]. The method starts by aligning and flattening the images and creating a 3-level multi-scale spatial pyramid. The edge and LBP histograms are then extracted from each block of every level of the pyramid. All the obtained histograms are concatenated into a global descriptor whose dimensions are reduced using PCA. Finally a SVM with an Radial Basis Function (RBF) kernel is used as classifier. The method achieved good results in detection OCT scan containing different pathology such as DME or AMD, with an AUC of 0.93 using a dataset of 326 OCT scans.

Lemaître *et al.* [14] proposed to use 2D and 3D LBP features extracted from denoised volumes and dictionary learning using the BoW models [15]. In the proposed method all the dictionaries are learned with same size of "visual words" ($k = 32$) and final descriptors are classified using RF classifier. The work described in this paper is an extension of our previous work [14]. In this research, beside the comparison of 2D and 3D features and global and local mapping, we also compare the effects of common pre-processing steps for OCT data (i.e., aligning, flattening beside denoising), study the optimal configuration regarding the BoW approach and finally the performance of different classifiers.

This paper is organized as follows: the proposed framework is explained in Sect. 2, while the experiments and results are discussed through Sect. 3 and Sect. 4. Finally, the conclusion and avenue for future directions are drawn in Sect. 5.

Table 1: Summary of the state-of-the-art methods.

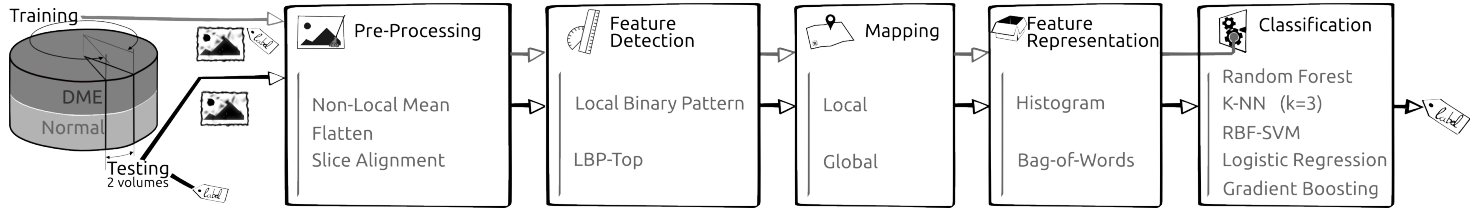| Ref	Diseases			Data size	Pre-processing				Features	Representation	Classifier	Evaluation	Results
	AMD	DME	Normal		De-noise	Flatten	Aligning	Cropping					
[11]	✓	✓	✓	45	✓	✓		✓	HOG		linear-SVM	ACC	86.7%,100%,100%
[12]	✓		✓	384					Texton	BoW, PCA	RF	AUC	0.984
[13]	✓	✓	✓	326		✓	✓		Edge, LBP	PCA	SVM-RBF	AUC	0.93
[14]		✓	✓	62	✓				LBP-LBP-TOP	PCA, BoW, histogram	RF	SE,SP	87.5%, 75%

5

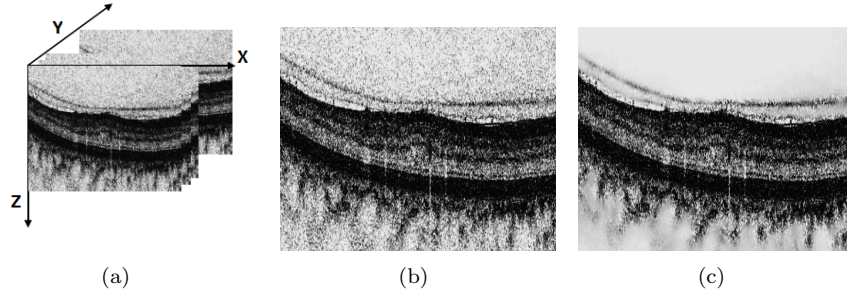Figure 2: Our proposed classification pipeline.

Figure 3: OCT: (a) Organization of the OCT data - (b) Original image - (c) NLM filtering. Note that the images have been negated for visualization purposes.

2. Materials and Methods

The proposed method, as well as, its experimental set-up for OCT volume classification are outlined in Fig. 2. The methodology is formulated as a standard classification procedure which consists of five steps. First, the OCT volumes are pre-processed as presented in details in Sect. 2.1. Then, LBP and LBP-TOP features are detected, mapped and represented as discussed in depth in Sect. 2.2, Sect. 2.3, and Sect. 2.4, respectively. Finally, the classification step is presented in Sect. 2.5.

2.1. Image pre-processing

This section describes the set of pre-processing techniques which aim at enhancing the OCT volume. The influence of these pre-processing methods and their possible combinations are extensively studied in Sect. 3.

2.1.1. Non-Local Means (NLM)

OCT images suffer from speckle noise, like other image modalities such as Ultra-Sound (US) [16]. The OCT volumes are enhanced by denoising each B-scan (i.e. each (x-z) slice) using the NLM [17], as shown in Fig. 3. NLM has been successfully applied to US images to reduce speckle noise and outperforms other common denoising methods [18]. NLM filtering preserves fine structures as well as flat zones, by using all the possible self-predictions that the image can provide rather than local or frequency filters such as Gaussian, anisotropic, or Wiener filters [17].
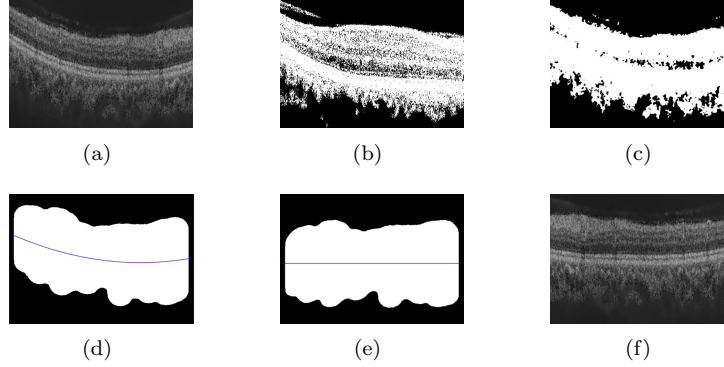
6

Figure 4: Flattening procedure: (a) original image, (b) thresholding, (c) median filtering, (d) curve fitting, (e) warping, (f) flatten image.

2.1.2. Flattening

Textural descriptors characterize spatial arrangement of intensities. However, the OCT scans suffer from large type of variations: inclination angles, positioning, and natural curvature of the retina [13]. Therefore, these variations have to be taken into account to ensure a consistent characterization of the tissue disposition, regardless of the location in the retina. This invariance can be achieved from different manners: (i) using a rotation invariant descriptor (cf. Sect. 2.2), or (ii) by unfolding the curvature of the retina. This latter correction is known as image flattening which theoretically consists of two distinct steps: (i) estimate and fit the curvature of the Retinal Pigment Epithelium (RPE) and (ii) warp the OCT volume such that the RPE becomes flat.

Our correction is similar to the one of Liu *et al.* [13]: each B-scan is thresholded using Otsu's method followed by a median filtering to detect the different retina layers (see Fig 4(c) and Fig 4(b)). Then, a morphological closing and opening is applied to fill the holes and the resulting area is fitted using a second-order polynomial (see Fig. 4(d)). Finally, the scan is warped such that the curve becomes a line as presented in Fig. 4(e) and Fig. 4(f).

7

2.1.3. Slice alignment

The flattening correction does not enforce an alignment through the OCT volume. Thus, in addition to the flattening correction, the warped curves of each B-scan are positioned at the same altitude in the z axis.

2.2. Feature detection

In this research, we choose to detect simple and efficient LBP texture features with regards to each OCT slice and volume. LBP is a texture descriptor based on the signs of the differences of a central pixel with respect to its neighboring pixels [19]. These differences are encoded in terms of binary patterns as in Eq. (1):

$$LBP_{P,R} = \sum_{p=0}^{P-1} s(g_p - g_c)2^p \; , \qquad s(x) = \begin{cases} 1 & \text{if } x \geq 0 \\ 0 & \text{otherwise} \end{cases} , \qquad (1)$$

where g_c, g_p are the intensities of the central pixel and a given neighbor pixel, respectively; P is the number of sampling points in the circle of radius R.

Ojala *et al.* further extended the original LBP formulation to achieve rotation invariance at the expense of limiting the texture description to the notion of circular "uniformity" [19]. Referring to the coordinate system defined in Fig. 3(a), the LBP codes are computed on each $(x$-$z)$ slice, leading to a set of LBP maps, a map for each $(x$-$z)$ slice.

Volume encoding is later proposed by Zhao *et al.* by computing LBP descriptors in three orthogonal planes, so called LBP-TOP [20]. More precisely, the LBP codes are computed considering the $(x$-$z)$ plane, $(x$-$y)$ plane, and $(y$-$z)$ plane, independently. Thus, three sets of LBP maps are obtained, one for each orthogonal plane.

In this work, we consider rotation invariant and uniform LBP and LBP-TOP features with various sampling points (i.e., $\{8, 16, 24\}$) with respect to different radius, (i.e., $\{1, 2, 3\}$). The number of patterns ($LBP_{\#pat}$) in regards with each configuration is reported in Table 2.

Table 2: Number of patterns ($LBP_{\#pat}$) for different sampling points and radius ($\{P, R\}$) of the LBP descriptor.

Sampling point for a radius ($\{P, R\}$)		
$\{8, 1\}$	$\{16, 2\}$	$\{24, 3\}$
$LBP_{\#pat}$ 10	18	26

Table 3: Size of a descriptor for an SD-OCT volume. d denotes the number of slices in the volume, N the number of 2D windows, and N' the number of 3D sub-volumes, respectively.

	Global mapping	Local mapping
LBP	$d \times LBP_{\#pat}$	$(N \times d) \times LBP_{\#pat}$
LBP-TOP	$1 \times (3 \times LBP_{\#pat})$	$N' \times (3 \times LBP_{\#pat})$

2.3. Mapping

The mapping stage is used to partition the previously computed LBP maps; for this work, two mapping strategies are defined: (i) *global* and (ii) *local* mapping.

The size of the feature descriptor is summarized in Table 3.

Global mapping extracts the final descriptors from the 2D feature image for LBP and 3D volume for LBP-TOP. Therefore, for a volume with d slices, the *global*-LBP mapping will lead to the extraction of d elements. While the *global*-LBP-TOP represents the whole volume as a single element. The *global* mapping for 2D images and 3D volume is shown in Fig. 5(a) and 5(b).

Local mapping extracts the final descriptors from a set of $(m \times m)$ 2D patches for LBP and a set of $(m \times m \times m)$ sub-volumes for LBP-TOP. Given N and N' the total number of 2D patches and 3D sub-volumes respectively, the *local*-LBP approach provides $N \times d$ elements, while *local*-LBP-TOP provides N' elements. This mapping is illustrated in Fig. 5(c) and 5(d).

2.4. Feature representation

Two strategies are used to describe each OCT volume's texture.
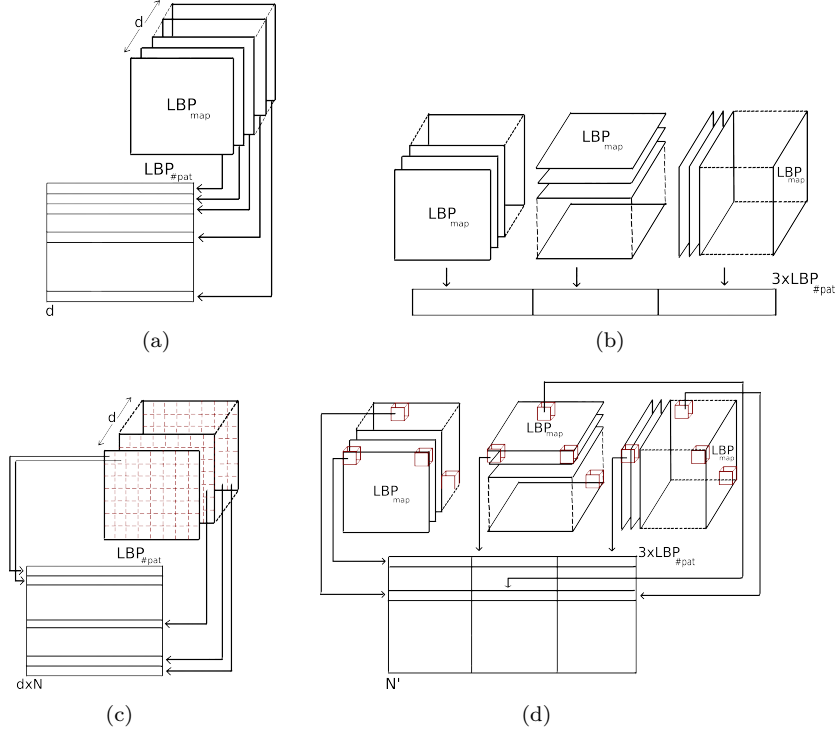
Figure 5: Graphical representation of the feature extraction: (a) extraction of LBP for global mapping - (b) extraction of LBP-TOP for global mapping - (c) extraction of LBP for local mapping - (d) extraction of LBP-TOP for local mapping.

Low-level representation The texture descriptor of an OCT volume is defined as the concatenation of the LBP histograms with the *global*-mapping. The LBP histograms are extracted from the previously computed LBP
₁₅₅ maps (see Sect. 2.2). Therefore, the LBP-TOP final descriptor is computed through the concatenation of the LBP histograms of the three orthogonal planes with the final size of $3 \times LBP_{\#pat}$. More precisely, an LBP histogram is computed for each set of LBP maps (x-z) plane, (x-y) plane, and (y-z) plane, respectively. Similarly, the LBP descriptor is de-
₁₆₀ fined through concatenation of the LBP histograms per each (x-z) slice with the final size of $d \times LBP_{\#pat}$.

High-level representation The concatenation of histograms employed in the low-level representation in conjunction with either *global*- or *local*-mapping

10

can lead to a high dimensional feature space. For instance, *local*-mapping results in a size of $N \times d \times LBP_{\#pat}$ for the final LBP descriptor and $N' \times LBP_{\#pat}$ for the final LBP-TOP descriptor, where N and N' the total number of 2D patches and 3D sub-volumes, respectively. High-level representation simplifies this high dimensional feature space into a more discriminant lower space. BoW approach is used for this purpose [15]. This model represents the features by creating a codebook or visual dictionary, from the set of low-level features. The set of low-level features are clustered using k-means to create the codebook with k clusters or visual words. After creating the codebook from the training set, the low-level descriptors are replaced by their closest word within the codebook. The final descriptor is a histogram of size k which represents the codebook occurrences for a given mapping.

2.5. Classification

The last step of our framework consists in the classification of SD-OCT volumes as normal or DME. For that matter, five different classifiers are used: (i) k-Nearest Neighbor (NN), (ii) Logistic Regression (LR) [21], (iii) Random Forest (RF) [22], (iv) Gradient Boosting (GB) [23, 24], and (v) Support Vector Machines (SVM) [25, 26]. Details regarding the parameters used in our experiments are provided in Sect. 3.

Table 4: The outline and summary of the performed experiments. $\sim$ indicate that common configuration applies.

	Dataset	Pre-processing	Features	Mapping	Representation	Classification	Evaluation
Common:	SERI	NLM	LBP,LBP-TOP $P = \{8, 16, 24\}$ $R = \{1, 2, 3\}$				Leave-One-Patient Out Cross-Validation (LOPO-CV) SE, SP
Baseline [14]: **Goal: Evaluation of features, mapping and representation**	+ Duke	$\sim$	$\sim$	*global* *local*	BoW Histogram	RF	+ comparison with [12]
Experiment#1: **Goal: Finding the optimum number of words**	$\sim$	+ F + F+A	$\sim$	*global* *local*	BoW $k \in K$	LR	+ACC, F1-score (F1)
Experiment#2: **Goal: Evaluation of different pre-processing and classifiers for high-level features**	$\sim$	+F +F+A	$\sim$	*global* *local*	BoW optimal k	3-NN RF SVM GB	$\sim$
Experiment#3: **Goal: Evaluation of different pre-processing and classifier for low-level features**	$\sim$	+F +F+A	$\sim$	*global*	Histogram	3-NN RF SVM GB	$\sim$

3. Experiments

A set of three experiments is designed to test the influence of the different blocks of the proposed framework in comparison to our previous work [14]. These experiments are designed such as:

(i) *Experiment #1* evaluates the effects of number of words used in BoW (high-level representation).

(ii) *Experiment #2* evaluates the effects of different pre-processing steps and classifiers on high-level representation.

(iii) *Experiment #3* evaluates the effects of different pre-processing steps and classifiers on low-level representation.

Table 4 reports the experiments which have been carried out in [14] as a baseline and outlines the complementary experimentation here proposed. The reminder of this section details the common configuration parameters across the experiments, while the detailed explanations are presented in the following subsections.

All the experiments are performed using a private dataset (see Sect. 3.1) and are reported as presented in Sect. 3.2. In all the experiments, LBP and LBP-TOP features are extracted using both *local* and *global*-mapping for different sampling points of 8, 16, and 24 for radius of 1, 2, and 3 pixels, respectively. The partitioning for *local*-mapping is set to (7×7) pixels patch for 2D LBP and $(7 \times 7 \times 7)$ pixels sub-volume for LBP-TOP.

3.1. SERI-Dataset

This dataset was acquired by the Singapore Eye Research Institute (SERI), using CIRRUS TM (Carl Zeiss Meditec, Inc., Dublin, CA) SD-OCT device. The dataset consists of 32 OCT volumes (16 DME and 16 normal cases). Each volume contains 128 B-scan with resolution of 512×1024 pixels. All SD-OCT images are read and assessed by trained graders and identified as normal or DME cases based on evaluation of retinal thickening, hard exudates, intraretinal cystoid space formation and subretinal fluid.

13

	Actual	
	A+	A-
P+	True Positive (TP)	False Positive (FP)
P-	False Negative (FN)	True Negative (TN)

Predicted

Figure 6: Confusion matrix with true and false positive detected samples (TP, FP) in the first row, from left to right and the false and true negative detected samples (FN, TN) in the second row, from left to right.

3.2. Validation

All the experiments are evaluated in terms of Sensitivity (SE) and Specificity (SP) using the LOPO-CV strategy, in line with [14]. SE and SP are statistics driven from the confusion matrix (see Fig. 6) as stated in Eq. (2). The SE evaluates the performance of the classifier with respect to the positive class, while the SP evaluates its performance with respect to negative class.

$$SE = \frac{TP}{TP + FN} \qquad SP = \frac{TN}{TN + FP} \qquad (2)$$

The use of LOPO-CV implies that at each round, a pair DME-normal volume is selected for testing while the remaining volumes are used for training. Subsequently, no SE or SP variance can be reported. However, LOPO-CV strategy has been adopted despite this limitation due to the reduced size of the dataset.

3.3. Experiment #1

This experiment intends to find the optimal number of words and its effect on the different configurations (i.e., pre-processing and feature representation), on the contrary to [14], where the codebook size was arbitrarily set to $k = 32$.

Several pre-processing strategies are used: (i) NLM, (ii) a combination of NLM and flattening (NLM+F), and (iii) a combination of NLM, flattening, and aligning (NLM+F+A). LBP and LBP-TOP descriptors are detected using the default configuration. Volumes are represented using BoW, where the codebook size ranging for $k \in \{10, 20, 30, \cdots, 100, 200, \cdots, 500, 1000\}$. Finally, the volumes are classified using LR. The choice of this linear classifier avoids that the

14

results get boosted by the classifier. In this manner, any improvement would be linked to the pre-processing and the size of the codebook.

The usual build of the codebook consists of clustering the samples in the feature space using k-means (see Sect. 2.4). However, this operation is rather computationally expensive and the convergence of the k-means algorithm for all codebook sizes is not granted. Nonetheless, Nowak *et al.* [27] pointed out that randomly generated codebooks can be used at the expenses of accuracy. Thus, the codebook are randomly generated since the final aim is to asses the influence of the codebook size and not the performance of the framework. For this experiment, the codebook building is carried out using random initialization using k-means++ algorithm [28], which is usually used as a k-means initialization algorithm.

For this experiment, SE and SP are complemented with ACC and F1 score (see Eq. (3)). ACC offers an overall sense of the classifier performance, and F1 illustrates the trade off between SE and precision. Precision or positive predictive value is a measure of algorithm exactness and is defined as a ratio of TP over the total predicted positive samples.

$$ACC = \frac{TP + TN}{TP + TN + FP + FN} \qquad F1 = \frac{2TP}{2TP + FP + FN} \qquad (3)$$

Appendix A - Table 6 shows the results obtained for the optimal dictionary size while the complete set of all ACC and F1 graphics can be found at [1]. According to the obtained results, it is observed that optimum number of words is smaller for *local*-LBP features in comparison to *local*-LBP-TOP and *global*-LBP, respectively. Using LR classifier, the best performances were achieved using *local*-LBP with 70 words (SE and SP of 75.0%) and *local*-LBP-TOP with 500 words (SE and SP of 75.0% as well). These results are highlighted in Appendix A - Table 6.

3.4. Experiment #2

This experiments explores the improvement associated with: (i) different pre-processing methods and (ii) using larger range of classifiers (i.e., linear and non-linear) on the high-level representation.

All the pre-processing stages are evaluated (NLM, NLM+F, and NLM+F+A). In this experiment, the codebooks for the BoW representation of LBP and LBP-TOP features are computed using regular k-means algorithm which is initialized using k-means++, where k is chosen according to the findings of *Experiment #1*. Finally, the volumes are classified using k-NN, RF, GB, and SVM. The k-NN classifier is used in conjunction with the 3 nearest-neighbors rule to classify the test set. The RF and GB classifier are trained using 100 un-pruned trees, while SVM classifier is trained using an RBF kernel and its parameters C, and γ are optimized through grid-search.

Complete list of the obtained results from this experiment are shown in Appendix A - Table 7. Despite that highest performances are achieved when NLM+F or NLM+F+A are used, most configurations decline when applied with extra pre-processing stages. The best results are achieved using SVM followed by RF.

3.5. Experiment #3

This experiment replicates the *Experiment #2* for the case of low-level representation of LBP and LBP-TOP features extracted using *global*-mapping.

The obtained results from this experiment are listed in Appendix A - Table 8. In this experiment, flattening the B-scan boosts the results of the best performing configuration. However, its effects is not consistent across all the configurations. Random forest has a better performance by achieving better SE (81.2%, 75.0%, 68.7%), while SVM achieve the highest SP (93.7%), see Appendix A - Table 8.

In terms of classifier, RF has a better performance than the others despite the fact that the highest SP is achieved using SVM.

16

Table 5: Summary of all the results. The best results for each experiment are denoted in bold.

Line	Experiment	Evaluation		Pre-processing	Feat. Detection				Mapping	Feat. Representation	Classifier	BoW
		SE	SP		Type	$\{8,1\}$	$\{16,2\}$	$\{24,3\}$				
1	#2	81.2	93.7	NLM+F	LBP	✓			local	High	SVM	✓
2	#2	75.0	93.7	NLM+F+A	LBP	✓			local	High	SVM	✓
3	#2	75.0	93.7	NLM	LBP	✓			local	High	SVM	✓
4	#2	75.0	100	NLM	LBP-TOP		✓		local	High	SVM	✓
5	#2	81.2	87.5	NLM	LBP-TOP	✓			local	High	SVM	✓
6	#2	81.2	87.5	NLM+F+A	LBP-TOP		✓		local	High	RF	✓
7	#2	81.2	81.2	NLM	LBP	✓			local	High	RF	✓
8	#3	81.2	81.2	NLM	LBP-TOP			✓	global	Low	RF	
9	#2	81.2	81.2	NLM+F	LBP-TOP	✓			local	High	SVM	✓
10	#3	81.2	81.2	NLM+F+A	LBP-TOP			✓	global	Low	GB	
11	#3	81.2	81.2	NLM+F	LBP-TOP			✓	global	Low	RF	
12	#2	75.0	87.5	NLM	LBP	✓			local	High	k-NN	✓
13	Lemaitre *et al.* [14]	75.0	87.5	NLM	LBP	✓			local	High	RF	✓
14	Lemaitre *et al.* [14]	75.0	87.5	NLM	LBP-TOP		✓		global	Low	RF	
15	#2	68.7	93.7	NLM	LBP	✓			global	High	RF	✓
16	#3	75	81.2	NLM+F+A	LBP-TOP			✓	global	Low	RF	
17	#2	68.7	81.2	NLM	LBP-TOP		✓		local	High	RF	✓
18	#3	62.5	93.7	NLM	LBP-TOP		✓		global	Low	SVM	
19	#3	68.7	87.5	NLM	LBP-TOP		✓		global	Low	RF	
20	#3	68.7	81.2	NLM	LBP-TOP				global	Low	RF	
21	#3	75.0	75.0	NLM	LBP-TOP				global	Low	RF	
22	#3	68.7	75.0	NLM+F	LBP-TOP	✓			global	Low	SVM	
23	#3	56.2	75.0	NLM	LBP			✓	global	Low	RF	
24	#3	56.2	75.0	NLM+F	LBP		✓		global	Low	k-NN	
25	#3	56.2	75.0	NLM+F+A	LBP		✓		global	Low	k-NN	
26	Venhuizen *et al.* [12]	61.5	58.8									

4. Results and discussion

Table 5 combines the obtained results from Sect. 3 with those reported by Lemaître *et al.* [14], while detailing the frameworks configurations. This table shows the achieved performances with SE higher than 55%.

The obtained results indicate that expansion and tuning of our previous framework improves the results. Tuning the codebook size, based on the finding of *Experiment #1*, leads to an improvement of 6% in terms of SE (see Table 5 at line 7 and 13). Furthermore, the fine tuning of our framework (see Sect. 2) also leads to an improvement of 6% in both SE and SP (see Table 5 at line 1 and 13). Our framework also outperforms the proposed method of [12] with an improvement of 20% and 36% in terms of SE and SP, respectively.

Note that although the effects of pre-processing are not consistent through all the performance, the best results are achieved with NLM +F and NLM +F+A configurations as pre-processing stages. In general, the configurations presented in *Experiment #2* outperform the others, in particular the high-level representation of locally mapped features with an SVM classifier. Focusing on the most desirable radius and sampling point configuration, smaller radius and sampling points are more effective in conjunction with local mapping, while global mapping benefit from larger radius and sampling points.

5. Conclusions

The work presented here addresses automatic classification of SD-OCT volumes as normal or DME. In this regard, an extensive study is carried out covering the (i) effects of different pre-processing steps, (ii) influence of different mapping and feature extraction strategies, (iii) impact of the codebook size in BoW, and (iv) comparison of different classification strategies.

While outperforming the previous studies [14, 12], the obtained results in this research showed the impact and importance of optimal codebook size, the potential of 3D features and high level representation of 2D features while extracted from local patches.

18

The strength of SVM while used along BoW approach and RF classifier while used with global mapping were shown. In terms of pre-processing steps, although the highest performances are achieved while alignment and flattening were used in the pre-processing, it was shown that the effects of these extra steps are not consistent for all the cases and do not guaranty a better performance.

Several avenues for future directions can be explored. The flattening method proposed by Liu *et al.* flattens roughly the RPE due to the fact that the RPE is not segmented. Thus, in order to have a more accurate flattening pre-processing, the RPE layer should be pre-segmented as proposed by Garvin *et al.* [29]. In this work, the LBP invariant to rotation was used and the number of pattern encoded is reduced. Once the data are flattened, the non-rotation invariant LBP could be studied since this descriptor encode more patterns. In addition to LBP, other feature descriptors can be included in the framework.

Acknowledgments

Conflict of interest statement

The authors declare no conflict of interest.

Appendix A   Complementary results for *Experiment #1 & #2 & #3*

19

Table 6: Experiment #1 - Optimum number of words for each configuration as a result of LR Classification, for high-level feature extraction of *global* and *local*-LBP, and *local*-LBP-TOP features with different pre-processing. The pre-processing includes: NF, F, and F+A. The achieved performances are indicated in terms of ACC, F1, SE, and SP

Features	Pre-processing	{8,1}					{16,2}					{24,3}				
		ACC%	F1%	SE%	SP%	W#	ACC%	F1%	SE%	SP%	W#	ACC%	F1%	SE%	SP%	W#
global-LBP																
	NF	81.2	78.5	68.7	93.7	500	62.5	58.0	56.2	62.5	80	62.5	62.5	62.5	62.5	80
	F	71.9	71.0	68.7	75.0	400	68.7	66.7	62.5	75.0	300	68.7	66.7	62.5	75.0	300
	F+A	71.9	71.0	68.7	75.0	500	71.9	71.0	68.7	75.0	200	75.0	68.7	68.7	68.7	500
local-LBP																
	NF	75.0	75.0	75.0	75.0	70	65.6	64.5	62.5	68.7	90	62.5	60.0	56.2	68.7	30
	F	75.0	73.3	68.7	81.2	30	71.8	61.0	68.7	75.0	70	62.5	62.5	62.5	62.5	100
	F+A	75.0	69.0	62.5	81.2	40	71.9	71.0	68.7	75.0	200	68.7	66.7	68.7	62.5	10
local-LBP-TOP																
	NF	68.7	68.7	68.7	68.7	400	75.0	75.0	75.0	75.0	500	71.9	71.0	68.7	75.0	60
	F	68.7	68.7	68.7	68.7	300	68.7	66.7	62.5	75.0	50	75.0	76.5	81.2	68.7	80
	F+A	75.0	73.3	68.7	81.2	100	75.0	73.3	68.7	81.2	90	75.0	69.0	62.5	81.2	70

Table 7: Experiment #2 - *k*-NN, SVM, RF, and GB classification with BoW for the *global* and *local* LBP and *local* LBP-TOP features with different pre-processing. The optimum number of words were selected based on experiment #1. The most relevant configurations are shaded. The configurations which their performances declines with additional pre-processing are shaded in light gray while those with the opposite behavior are shaded with darker gray color. The highest results which are specified in Table 5 are highlighted in **bold**.

Features	Pre-processing	*k*-NN {8, 1}		{16, 2}		{24, 3}		SVM {8, 1}		{16, 2}		{24, 3}	
		SE%	SP%	SE%	SP%	SE%	SP%	SE%	SP%	SE%	SP%	SE%	SP%
global-LBP													
	NF	43.7	93.7	43.7	87.5	43.7	62.5	68.7	87.5	62.5	62.5	50.0	56.2
	F	43.7	56.2	50.0	75.0	62.5	56.2	56.2	56.2	56.2	75.0	56.2	68.7
	FA	56.2	62.5	43.7	81.2	68.7	56.2	56.2	68.7	68.7	68.7	56.2	75.0
local-LBP													
	NF	**75.0**	**87.5**	50.0	68.7	43.7	43.7	**75.0**	**93.7**	50.0	75.0	56.2	56.2
	F	56.2	56.2	50.0	50.0	50.0	43.7	**81.2**	**93.7**	68.7	68.7	68.7	75.0
	FA	56.2	43.7	50.0	75.0	50.0	62.5	**75.0**	**93.7**	75.0	68.7	68.7	68.7
local-LBP-TOP													
	NF	56.2	75.0	56.2	75.0	62.5	56.2	**81.2**	**87.5**	**75.0**	**100**	56.2	75.0
	F	62.5	43.7	37.5	68.7	43.7	62.5	**81.2**	**81.2**	75.0	68.7	81.2	68.7
	F+A	56.2	56.2	68.7	50.0	43.7	62.5	62.5	75.0	68.7	75.0	62.5	81.2

Features	Pre-processing	RF 8^{riu2}		16^{riu2}		24^{riu2}		GB 8^{riu2}		16^{riu2}		24^{riu2}	
		SE%	SP%	SE%	SP%	SE%	SP%	SE%	SP%	SE%	SP%	SE%	SP%
global-LBP													
	NF	**68.7**	**93.7**	43.7	62.5	50.0	68.7	56.2	50.0	37.5	31.2	50.0	43.7
	F	56.2	50.0	56.2	75.0	50.0	75.0	50.0	56.2	56.2	75.0	43.7	62.5
	FA	68.7	50.0	56.2	62.5	62.5	56.2	56.2	50.0	68.7	50.0	43.7	75.0
local-LBP													
	NF	**81.2**	**81.2**	62.5	56.2	56.2	56.2	75.0	62.5	68.7	87.5	50.0	75.0
	F	56.2	81.2	62.5	68.7	68.7	62.5	68.7	75.0	50.0	75.0	50.0	62.5
	FA	68.7	62.5	62.6	68.7	43.7	43.7	56.2	50.0	68.7	56.2	50.0	50.0
local-LBP-TOP													
	NF	68.7	62.5	**68.7**	**81.2**	68.7	68.7	37.5	68.7	62.5	81.2	62.5	50.0
	F	50.0	62.5	62.5	62.5	43.7	75.0	50.0	56.2	43.7	62.5	50.0	62.5
	F+A	50.0	62.5	**81.2**	**87.5**	50.0	68.7	56.2	62.5	81.2	68.7	75.0	68.7

Table 8: Experiment #3 - Classification results obtained from low-level representation of global LBP and LBP-TOP features with different pre-processing. Pre-processing steps include: NF, F, F+A. Different classifiers such as RF, GB, SVM, and k-NN are used. The most relevant configurations are shaded. The configurations which their performances declines with additional pre-processing are shaded in light gray while those with the opposite behavior are shaded with darker gray color. The highest results which are specified in Table 5 are highlighted in **bold**.

Features	Pre-processing	k-NN {8,1}		{16,2}		{24,3}		SVM {8,1}		{16,2}		{24,3}	
		SE%	SP%	SE%	SP%	SE%	SP%	SE%	SP%	SE%	SP%	SE%	SP%
global-LBP													
	NF	37.5	50.0	25.0	50.0	37.5	68.7	56.2	62.5	56.2	43.7	56.2	68.7
	F	62.5	50.0	56.2	75.0	62.5	68.7	75.0	68.7	62.5	62.5	62.5	68.7
	FA	56.2	50.0	56.2	75.0	62.5	68.7	75.0	68.7	62.5	62.5	62.5	68.7
global-LBP-TOP													
	NF	31.2	93.7	37.5	100.0	37.5	81.2	62.5	75.0	**62.5**	**93.7**	56.2	87.5
	F	50.0	56.2	56.2	75.0	56.2	62.5	68.7	75.0	43.7	68.7	68.7	56.2
	F+A	75.0	43.7	56.2	43.7	68.7	50.0	68.7	62.5	62.5	56.2	56.2	68.7

Features	Pre-processing	RF 8^{riu2}		16^{riu2}		24^{riu2}		GB 8^{riu2}		16^{riu2}		24^{riu2}	
		SE%	SP%	SE%	SP%	SE%	SP%	SE%	SP%	SE%	SP%	SE%	SP%
global-LBP													
	NF	43.7	62.5	43.7	62.5	56.2	75	43.7	43.7	43.7	37.5	37.5	31.25
	F	56.2	56.2	68.7	62.5	62.5	68.7	25	56.2	50.0	43.7	25.0	43.7
	F+A	65.2	56.2	50.0	50.0	56.2	68.7	43.75	62.5	62.5	50.0	31.2	31.2
global-LBP-TOP													
	NF	56.2	68.7	**68.7**	**87.5**	**68.7**	**81.2**	68.7	68.7	75.0	50.0	56.2	43.7
	F	56.2	62.5	81.2	68.7	**81.2**	**81.2**	56.2	62.5	62.5	68.7	68.7	81.2
	F+A	68.7	62.5	75.0	68.7	**75.0**	**81.2**	56.2	43.7	62.5	62.5	**75.0**	**75.0**

References

[1] G. Lemaitre, M. Rastgoo, J. Massich, retinopathy: Jo-omia-2015 (Nov. 2015). doi:10.5281/zenodo.34277.

URL http://dx.doi.org/10.5281/zenodo.34277

[2] S. Sharma, A. Oliver-Hernandez, W. Liu, J. Walt, The impact of diabetic retinopathy on health-related quality of life, Current Opinion in Ophtalmology 16 (2005) 155–159.

[3] S. Wild, G. Roglic, A. Green, R. Sicree, H. King, Global prevalence of diabetes estimates for the year 2000 and projections for 2030, Diabetes Care 27 (5) (2004) 1047–1053.

[4] Early Treatment Diabetic Retinopathy Study Group, Photocoagulation for diabetic macular edema: early treatment diabetic retinopathy study report no 1, JAMA Ophthalmology 103 (12) (1985) 1796–1806.

[5] M. R. K. Mookiah, U. R. Acharya, C. K. Chua, C. M. Lim, E. Ng, A. Laude, Computer-aided diagnosis of diabetic retinopathy: A review, Computers in Biology and Medicine 43 (12) (2013) 2136–2155.

[6] E. Trucco, A. Ruggeri, T. Karnowski, L. Giancardo, E. Chaum, J. Hubschman, B. al Diri, C. Cheung, D. Wong, M. Abramoff, G. Lim, D. Kumar, P. Burlina, N. M. Bressler, H. F. Jelinek, F. Meriaudeau, G. Quellec, T. MacGillivray, B. Dhillon, Validation retinal fundus image analysis algorithms: issues and proposal, Investigative Ophthalmology & Visual Science 54 (5) (2013) 3546–3569.

[7] Y. T. Wang, M. Tadarati, Y. Wolfson, S. B. Bressler, N. M. Bressler, Comparison of Prevalence of Diabetic Macular Edema Based on Monocular Fundus Photography vs Optical Coherence Tomography, JAMA Ophthalmology (2015) 1–7.

23

[8] S. J. Chiu, X. T. Li, P. Nicholas, C. A. Toth, J. A. Izatt, S. Farsiu, Automatic segmentation of seven retinal layers in sd-oct images congruent with expert manual segmentation, Optic Express 18 (18) (2010) 19413–19428.

[9] R. Kafieh, H. Rabbani, M. D. Abramoff, M. Sonka, Intra-retinal layer segmentation of 3d optical coherence tomography using coarse grained diffusion map, Medical Image Analysis 17 (2013) 907–928.

[10] P. P. Srinivasan, L. A. Kim, P. S. Mettu, S. W. Cousins, G. M. Comer, J. A. Izatt, S. Farsiu, Fully automated detection of diabetic macular edema and dry age-related macular degeneration from optical coherence tomography images, Biomedical Optical Express 5 (10) (2014) 3568–3577.

[11] F. G. Venhuizen, B. van Ginneken, B. Bloemen, M. J. P. P. van Grisven, R. Philipsen, C. Hoyng, T. Theelen, C. I. Sanchez, Automated age-related macular degeneration classification in OCT using unsupervised feature learning, in: SPIE Medical Imaging, Vol. 9414, 2015, p. 94141l.

[12] Y.-Y. Liu, M. Chen, H. Ishikawa, G. Wollstein, J. S. Schuman, R. J. M., Automated macular pathology diagnosis in retinal oct images using multi-scale spatial pyramid and local binary patterns in texture and shape encoding, Medical Image Analysis 15 (2011) 748–759.

[13] G. Lemaitre, M. Rastgoo, J. Massich, S. Sankar, F. Meriaudeau, D. Sidibe, Classification of SD-OCT volumes with LBP: Application to dme detection, in: Medical Image Computing and Computer-Assisted Intervention (MICCAI), Ophthalmic Medical Image Analysis Workshop (OMIA), 2015.

[14] J. Sivic, A. Zisserman, Video google: a text retrieva approach to object matching in videos, in: IEEE ICCV, 2003, pp. 1470–1477.

[15] J. M. Schmitt, S. H. Xiang, K. M. Yung, Speckle in optical coherence tomography, Journal of biomedical optics 4 (1) (1999) 95–105.

[16] A. Buades, B. Coll, J.-M. Morel, A non-local algorithm for image denoising, in: Computer Vision and Pattern Recognition, 2005. CVPR 2005. IEEE Computer Society Conference on, Vol. 2, IEEE, 2005, pp. 60–65.

[17] P. Coupe, P. Hellier, C. Kervrann, C. Barillot, Nonlocal means-based speckle filtering for ultrasound images, IEEE TIP (2009) 2221–2229.

[18] T. Ojala, M. Pietikäinen, T. Mäenpää, Multiresolution gray-scale and rotation invariant texture classification with local binary patterns, Pattern Analysis and Machine Intelligence, IEEE Transactions on 24 (7) (2002) 971–987.

[19] G. Zhao, T. Ahonen, J. Matas, M. Pietikäinen, Rotation-invariant image and video description with local binary pattern features, Image Processing, IEEE Transactions on 21 (4) (2012) 1465–1477.

[20] D. R. Cox, The regression analysis of binary sequences, Journal of the Royal Statistical Society. Series B (Methodological) (1958) 215–242.

[21] L. Breiman, Random forests, Machine learning 45 (1) (2001) 5–32.

[22] J. H. Friedman, Stochastic gradient boosting, Computational Statistics & Data Analysis 38 (4) (2002) 367–378.

[23] G. Lemaitre, J. Massich, R. Marti, J. Freixenet, J. C. Vilanova, P. M. Walker, D. Sidibe, F. Meriaudeau, A boosting approach for prostate cancer detection using multi-parametric mri, in: International Conference on Quality Control and Artificial Vision (QCAV2015), SPIE, 2015.

[24] V. Vapnik, A. J. Lerner, Generalized portrait method for pattern recognition, Automation and Remote Control 24 (6) (1963) 774–780.

[25] A. Aizerman, E. M. Braverman, L. I. Rozoner, Theoretical foundations of the potential function method in pattern recognition learning, Automation and Remote Control 25 (1964) 821–837.

[26] E. Nowak, F. Jurie, B. Triggs, Sampling strategies for bag-of-features image classification, in: Computer Vision–ECCV 2006, 2006, pp. 490–503.

[27] D. Arthur, S. Vassilvitskii, k-means++: The advantages of careful seeding, in: Proceedings of the eighteenth annual ACM-SIAM symposium on Discrete algorithms, Society for Industrial and Applied Mathematics, 2007, pp. 1027–1035.

[28] M. Garvin, M. Abramoff, X. Wu, S. Russell, T. Burns, M. Sonka, Automated 3-d intraretinal layer segmentation of macular spectral-domain optical coherence tomography images, Medical Imaging, IEEE Transactions on 28 (9) (2009) 1436–1447.